Unveiling the thermal stability of diketopyrrolopyrrole-based terpolymers: a key element for enhanced efficiency and stability of organic solar cells

NJC

ROYAL SOCIETY OF CHEMISTRY

PAPER

View Article Online
View Journal | View Issue

Cite this: *New J. Chem.*, 2024, **48**, 10201

Unveiling the thermal stability of diketopyrrolopyrrole-based terpolymers: a key element for enhanced efficiency and stability of organic solar cells

Leonato Tambua Nchinda,[a] Zewdneh Genene,[b] Wendimagegn Mammo,[c] Newayemedhin A. Tegegne[d] and Tjaart P. J. Krüger *[ae]

With the advent of novel polymers, organic solar cell (OSC) research has evolved significantly over the past decade. The molecular engineering of terpolymers has allowed for simple morphological control in binary devices over ternary blends, with the highest power conversion efficiencies (PCEs) exceeding 18%. However, research on the stability of OSCs is still lagging behind. In this regard, we examined the thermal stability of a series of terpolymers comprising one electron donor (thienyl-substituted benzodithiophene, BDTT) and two types of electron acceptors namely fluorobenzotriazole (FTAZ) and thienothiophene-capped diketopyrrolopyrrole (TTDPP) and their blends with $PC_{71}BM$. The terpolymers demonstrated broad absorbance ranging from below 350 nm to 900 nm. The thermal stability of the terpolymers was investigated as pristine thin films and as bulk heterojunction (BHJ) films of the terpolymers blended with $PC_{71}BM$ by heating at 85 °C. We observed that thermal degradation had no sizeable effect on the properties of the pristine terpolymers while the blended films demonstrated significant changes in their morphology due to the inclusion and aggregation of $PC_{71}BM$. After thermal annealing at 85 °C, the width of the symmetric C=C stretching Raman mode and the C=C/C–C intensity ratio of pristine terpolymers and terpolymer:$PC_{71}BM$ thin films revealed that incorporation of the FTAZ acceptor improves the thermal stability of the BHJ active layers. Furthermore, prolonged thermal annealing times (>3 hours) resulted in the development of $PC_{71}BM$ aggregates and terpolymer decomposition with no evident changes in the molecular and chemical structure of the terpolymers. Our findings indicate that by gradually annealing the blended films using an appropriate annealing time, the diffusion of $PC_{71}BM$ molecules to form aggregates can be carefully regulated, resulting in a nanostructure critical to the efficiency of organic solar cells.

Received 11th November 2023,
Accepted 29th April 2024

DOI: 10.1039/d3nj05210a

rsc.li/njc

1 Introduction

After the first publication on bilayer solar cells in 1986,[1] research on organic solar cells (OSCs) has witnessed continual growth due to their unique features of low cost, lightweight, broad spectral absorption, and facile solution-based manufacturing with mechanical flexibility. The power conversion efficiency (PCE) has been greatly improved by employing low-bandgap materials, improving device topologies, and manipulating the morphology of active layers.[2–7] Although the reported PCEs often meet the basic requirements for commercial applications, the low stability of OSCs remains a key hurdle to commercialisation. Among the factors that stimulate the performance degradation of OSCs are oxygen, water, UV radiation, and high temperatures.[6,8,9]

When exposed to continuous irradiation, OSCs become susceptible to thermal degradation, which reduces their stability and PCE. The stability of the device depends on the thermal characteristics of the materials, such as the glass transition temperature, crystallisation, and phase transition. The primary mechanisms of degradation include the diffusion of electrodes, buffer layers, and active layer materials. These modifications alter the morphology of the active layer and can impede the charge generation process. Changes in the miscibility and crystallisation of active-layer components upon thermal degradation can lead to the evolution of a network that is not conducive to charge generation.[10,11] A low degree of miscibility between the donor and acceptor materials can cause them

[a] *Department of Physics, University of Pretoria, Private Bag X20, Hatfield, 0028, South Africa. E-mail: tjaart.kruger@up.ac.za*
[b] *Department of Chemistry and Chemical Engineering, Chalmers University of Technology, Gothenburg, SE412 96, Sweden*
[c] *Department of Chemistry, Addis Ababa University, Addis Ababa, 33658, Ethiopia*
[d] *Department of Physics, Addis Ababa University, Addis Ababa, 1176, Ethiopia*
[e] *National Institute for Theoretical and Computational Sciences (NITheCS), South Africa*

to aggregate and form larger-sized domains or clusters that may be larger than the charge transport or exciton diffusion lengths.[12,13]

Recently, great improvements have been made in the field of OSC research. An important breakthrough came with the introduction of the random terpolymerisation strategy aimed at creating ''ideal'' low-bandgap copolymers. This strategy combines three distinct monomers with the goal of broadening the absorption spectrum for improved photon harvesting, fine-tuning molecular energy levels through monomer composition control, and regulating the molecular packing and crystallinity of the resulting copolymers by selecting appropriate comonomers.[14–16] Diketopyrrolopyrrole (DPP) has been one of the most prominent acceptor-building components in both donor–acceptor (D–A) alternating copolymers and D–A–D terpolymers due to its exceptional electron-withdrawing capabilities, high extinction coefficient, and molecular planarity.[17–20] The intense absorbance of DPP-based alternating copolymers in the 500 nm to 950 nm wavelength range and their relatively moderate absorbance in the wavelength range of 350 nm to 500 nm allow for the identification of high-bandgap polymers with complementary absorption for the design of terpolymer-based OSCs with improved overall coverage of the solar spectrum. Despite the fact that it has already been used in standard D–A alternating copolymers,[20–23] thienothiophene-capped DPP (TTDPP) has been given little attention in comparison to thiophene-capped DPP (TDPP) and pyridine-capped DPP (PyDPP). So far, TDPP and PyDPP have been employed in conjunction with other acceptors for the development of terpolymer systems, and OSCs developed using these materials have exhibited PCEs of more than 8%.[23–28] However, since TTDPP-based alternating copolymers exhibit poor absorption in the short wavelength region (UV and blue regions), acceptors with complementing absorption are attractive partners in a terpolymer strategy. Previous research has shown that high-bandgap copolymers containing a fluorinated benzotriazole (FTAZ) moiety absorb strongly between 400 nm and 650 nm.[15] Furthermore, because of its rigid and planar conjugated structure, benzo[1,2-*b*:4,5-*b*′]dithiophene (BDT) has been one of the most extensively employed electron-donating building blocks for OSC development.[29–32] Hence, terpolymerization can be a viable route for improving the absorption width of these polymers. Despite the above-mentioned merits, terpolymer-based OSCs still exhibit low photovoltaic performance and poor long-term stability when compared with highly crystalline D–A copolymer-based OSCs. It is therefore desirable to synthesise terpolymer-based OSCs with simultaneously enhanced photovoltaic performance and long-term thermal and photochemical stability.

We recently reported three terpolymers by using two acceptors (TTDPP and FTAZ) and one donor (BDT) with a high thermal decomposition temperature of >420 °C and a PCE of 5.7% and 6.3% in $PC_{71}BM$- and IECO-4F-based devices, respectively by changing the ratios of the acceptors in the backbone of the terpolymers.[33] This high performance obtained by tuning the ratio of TTDPP and FTAZ was due to the broadening of the absorption spectrum of the terpolymers that extends between 300 and 900 nm. Interestingly, in our work, we could see that the terpolymers could afford a low energy loss of $\sim$0.8 V. However, the thermal stability of these terpolymers is yet to be investigated. Prior research on thermal annealing of similar BHJ solar cells has mostly focused on the investigation of as-cast and treated devices at optimal temperatures, evaluating the influence on device characteristics such as open circuit voltage (V_{oc}), short-circuit current (J_{sc}), and the resulting PCE. However, since charge photogeneration mainly occurs in the active layer of an OSC, understanding the degradation mechanisms in the active layer is essential to preparing both high-performing and stable devices. Thermal stress in solar cell devices is unavoidable due to overheating of the device during long periods of irradiation under normal working conditions. Hence, establishing the effect of thermal stress on an OSC's active-layer nanostructures, chemical stability, and absorbance will assist in controlling thermally-induced degradation.[9,16] For example, using *in situ* Raman and optical microscopy, Veerender *et al.* observed the formation of $PC_{71}BM$ aggregates after heating P3HT:$PC_{71}BM$ active layers at higher temperatures.[9] We, therefore, assert that important physical modifications may be observed after heating the DPP-based terpolymer active layers at elevated temperatures and its implications on phase separations and in particular photocurrent generation can give significant insight into the long-term device performance.

In this contribution, we continued our work followed by the successful PCE in the terpolymers synthesised before,[33] mainly focusing on their thermal stability. Our study focused on the thermally-induced degradation of pristine terpolymers namely, **P1**, **P2**, and **P3** with FTAZ : TTDPP ratios of 1 : 3, 1 : 1, and 3 : 1, respectively (structure shown in Scheme 1) and their optimised bulk-heterojunction (BHJ) blend films with $PC_{71}BM$ with a polymer-acceptor ratio of 1 : 1.5. More specifically, the relationship between thermal annealing duration and morphological instability of donor:acceptor BHJ films is investigated using absorption spectroscopy, Raman spectroscopy, transmission electron microscopy, atomic force microscopy, X-ray diffraction (XRD), and time-resolved fluorescence. We evaluated the influence of thermal annealing at 85 °C for 3 and 24 h on the morphology of three DPP-based terpolymer:$PC_{71}BM$ blends and established that the initially optimised morphology does not remain stable over long-term operation or storage at higher temperatures. The choice of 85 °C accelerated the degradation process, allowing for the assessment of the stability and durability of the active layers under conditions that may be encountered in real-world applications. However, unlike other OSC active layer materials that degrade upon thermal annealing, we observed no clear molecular or chemical changes in the terpolymer:$PC_{71}BM$ active layers, which is a unique characteristic required for the development of more efficient and stable OSCs.

2 Experimental

2.1 Materials

The molecular structure of the random terpolymers **P1–P3** is depicted in Scheme 1.[33] The chemical configuration of the

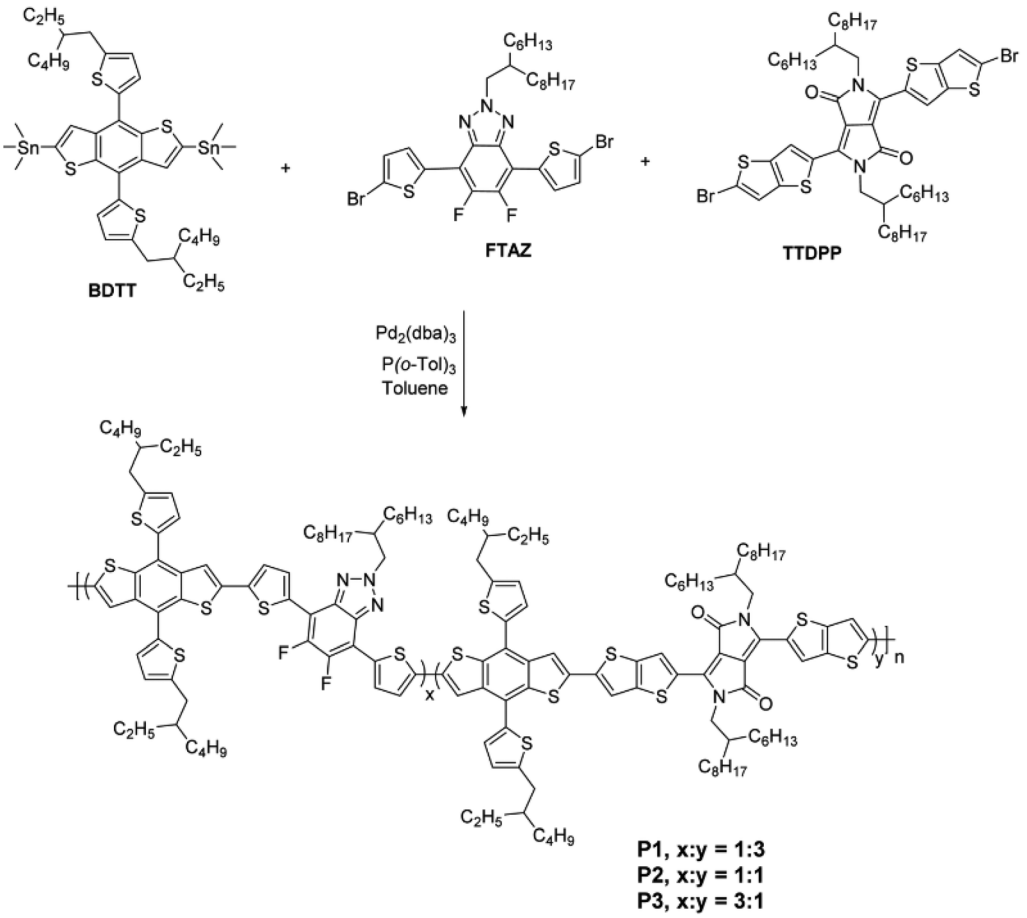

Scheme 1 Molecular structure of terpolymers **P1–P3** showing their constituent parts.

three terpolymers is D–A1–D–A2 (Scheme 1), with FTAZ (A1) and TTDPP (A2) serving as the first and second electron-accepting moieties and thienyl-substituted benzodithiophene (BDTT) serving as the electron-donating (D) unit. By altering the ratio of the FTAZ and TTDPP units, the absorption spectra and energy levels of the terpolymers were modified.[33] To explore the influence of these different acceptor concentrations on the optoelectronic characteristics and thermal stability of prospective OSC active layers, three different FTAZ : TTDPP ratios, *i.e.*, 1 : 3, 1 : 1, and 3 : 1 for **P1**, **P2**, and **P3**, respectively, were utilised, as shown in Scheme 1. Regioregular[6,6]-phenyl-C_{71}-butyric acid methyl ester ($PC_{71}BM$) was purchased from Ossila and used as received without any further purification. Glass substrates were used for solar cell active layer fabrication. 1,2-Dichlorobenzene (DCB) was acquired from Sigma-Aldrich and utilised as supplied.

2.2 Preparation of pristine terpolymer and P1–P3:$PC_{71}BM$ thin films

Thin films of pristine terpolymers and BHJ blends of **P1–P3**:$PC_{71}BM$ were made according to the following preparation guidelines. In an ultrasonic bath, the glass substrates were cleaned successively in a soap solution, deionised water, acetone, and isopropanol for 10 minutes each. Thereafter, the substrates were blasted dry using nitrogen gas. The active layers, consisting of a blend of each terpolymer and $PC_{71}BM$ in *o*-DCB, were spin-coated on the glass substrates at 1200 rpm. Using a profilometer, the thicknesses of the as-cast **P1–P3**:$PC_{71}BM$ thin films were measured as 138.17 nm, 102.50 nm, and 92.83 nm for the **P1**-, **P2**-, and **P3**-based active layers, respectively. To achieve total dissolution, the **P1–P3**:$PC_{71}BM$ solutions were stirred for 3 h at 50 °C. The **P1–P3**:$PC_{71}BM$ ratio was 1 : 1.5 with a mass concentration of 25 mg mL^{-1} in *o*-DCB solvent. Finally, thermal annealing of the thin films was performed in an oven at 85 °C for 3 h and 24 h.

2.3 Spectroscopic and morphological characterisation

Absorption spectra of pristine and blended thin films were recorded using a PerkinElmer Lambda 19 UV-VIS-NIR spectrophotometer. Raman spectra were acquired using a WITec alpha 300 correlative Raman-AFM microscope with a 532 nm Ar^+ laser as the excitation source. The laser power and acquisition duration were chosen such that the thin films did not suffer from photodegradation. A 100× objective lens focused the laser beam onto the sample into a spot size of roughly 5 μm. The acquired spectra were averaged over five accumulated single spectra and fitted with Lorentzian functions to calculate the peak location, full-width at half-maximum (FWHM), and

intensity ratio of the bands of interest. Atomic force microscopy (AFM) images were acquired in contact mode using a scanning probe microscope (VEECO atomic force microscope) and analysed using the nanoscope software. The morphology of the films was additionally measured using a transmission electron microscope (JEOL field emission electron microscope JEM-2100F). The observed trends were supported with solid-state structural characterisation using X-ray diffraction (PANalytical X'Pert Pro) and the stability of the active layers was further characterised using time-resolved fluorescence through time-correlated single-photon counting (TCSPC). The home-built TCSPC experimental setup described in ref. 34 was equipped with a supercontinuum picosecond pulsed laser source (SuperK EVO, NKT Photonics). The laser beam was sent through a 632.8-nm band-pass filter (FLH633-1, Thorlabs) to produce an optically narrow excitation beam centred about 633 nm, which was subsequently reflected by a dichroic mirror (FF649-Di01-25 × 36 Semrock Brightline) into a water-immersion objective (Nikon CFI NIR Apochromat 60×, NA 1.0). Fluorescence from the sample was focussed through a 75-μm pinhole and fluorescence filter (FELH0650, Thorlabs) to block scattered excitation light, and measured by a single-photon avalanche diode (COUNT-T100, Laser Components) coupled to a Becker & Hickl GmbH TCSPC module (SPC-130 EM). Using a custom-written LabVIEW (National Instruments) script, each sample was measured for 60 seconds. The instrument response function (IRF) was measured at the same excitation wavelength using back-reflected light. All measurements were done at room temperature.

3 Results and discussion

3.1 Absorption of pristine terpolymers and P1–P3:$PC_{71}BM$ thin films

The terpolymers exhibited broad absorption, extending from below 350 nm to above 900 nm (Fig. 1(a)–(c)). The absorption spectrum can be divided into three main bands, with the first band between 350 nm and 450 nm attributed to terpolymer backbone π−π* transitions and intramolecular charge transfer from the donor, BDTT, to the two acceptors, FTAZ and TTDPP, as shown in Fig. 1. This multiple-band profile is a common feature of alternating co-/terpolymers.[35] The absorption of the terpolymers could be effectively broadened by increasing the TTDPP concentration in their backbone (**P3** < **P2** < **P1**), while stronger absorption in the region between 450 and 600 nm could be achieved with a higher FTAZ ratio (**P1** < **P2** < **P3**) due to its lower electron-accepting nature.[15] This confirms that rational coupling of the moieties in the terpolymers could be an effective route to enhance the photocurrent in the resultant OSCs.[16,33]

Comparison of the absorption spectra of the BHJ **P1–P3**:$PC_{71}BM$ thin films (Fig. 1, right) with those of the pristine terpolymers (Fig. 1, left) indicates that $PC_{71}BM$ absorbs strongly below ∼500 nm, while the absorption of the terpolymers dominates above this wavelength. Because $PC_{71}BM$'s absorption is greatest below ∼300 nm where the solar spectral

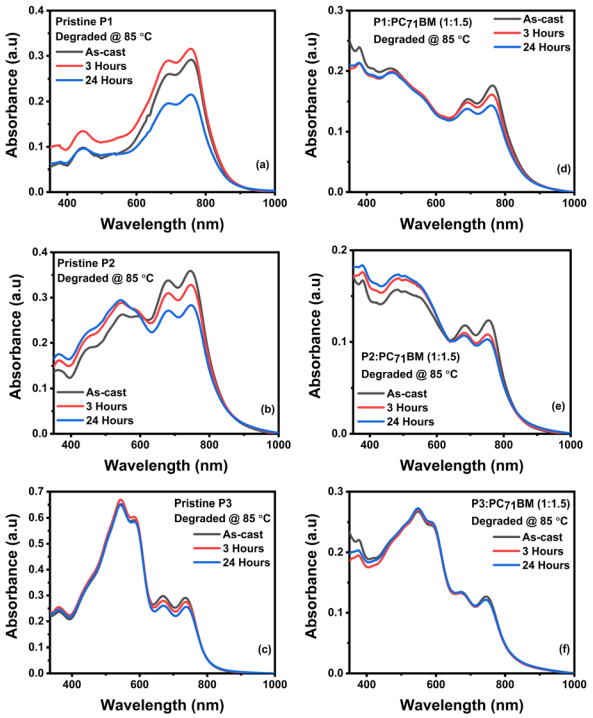

Fig. 1 Room-temperature absorption spectra of pristine terpolymers (a–c) and **P1–P3**:$PC_{71}BM$ thin films (d–f) degraded at 85 °C for 3 and 24 h.

intensity is low, its contribution to exciton generation in the blended films plays a less important role than its electron transport property.[36]

The absorption spectra of the pristine and the BHJ films of the terpolymers with $PC_{71}BM$ were recorded at 85 °C to monitor their thermal stability as shown in Fig. 1. Beginning with the absorption spectra of the pristine **P1** film (Fig. 1, top left), after 3 h of thermal annealing, there was an increase in the absorption intensity indicating an increased interchain stacking of **P1** terpolymer chains. After 24 h of thermal annealing, the absorption was significantly decreased due to the bleaching of the **P1** backbone.[37–39] Notably, after 24 h of thermal annealing, the decrease in absorption intensity in the red region of the spectrum was faster than that in the blue region, which remained almost the same as that of the as-cast film. This indicates that for the **P1**-based films, thermal annealing reduced the intramolecular coupling between the donor and acceptors so that the ICT above 600 nm is bleached while the π−π* region remained the same.[37–39] Similarly, the absorbance of the **P2** film in the region below 600 nm increased while it decreased in the region above 600 nm during the aging time confirming the partial decoupling of the donor and acceptor units in the terpolymer backbone.[8,40] On the contrary, the pristine **P3** film, which contains the highest FTAZ concentration, did not exhibit notable thermally-induced changes, confirming that the incorporation of FTAZ serves as a suitable route for enhancing thermal stability.[33] It is worth noting that no blue-shift in the absorption of any of the terpolymers occurred, indicating no or only minimal chain scission. This is consistent with the superior thermal properties of these

terpolymers with decomposition temperature above 420 °C, as shown earlier.[33]

Interestingly, thermal degradation occurred more slowly in the blends (Fig. 1, left) than in the pristine terpolymer films (Fig. 1, right). The superior stability of the **P1–P3**:$PC_{71}BM$ thin films could be ascribed to the thermal screening effect of $PC_{71}BM$ since it has a higher density than the terpolymers and resides at the top of the films.[8,40,41] However, as demonstrated below, longer annealing times resulted in the segregation of $PC_{71}BM$ molecules from the BHJ blends, forming clusters that are suggested to be detrimental to the morphology and charge dynamics of the prospective OSCs.

3.2 Raman spectroscopy of pristine terpolymers and blend films

Fig. 2 depicts the typical room-temperature Raman spectra of the as-cast terpolymers, $PC_{71}BM$, and **P1–P3**:$PC_{71}BM$ thin films. Due to their sensitivity to π-electron delocalisation, the symmetric C=C ring stretching (peaking at 1440 cm^{-1}) and the skeletal C–C stretching (peaking at 1395 cm^{-1}) modes are of special interest.[42,43] It is well-documented that molecular ordering and excitation wavelength have a significant impact on the peak position, line width, and intensity of the symmetric C=C stretching Raman mode, with resonant excitation providing better Raman results than non-resonant excitation.[42–44] Owing to its sensitivity to conjugation length, the Raman shift of the terpolymer C=C mode may therefore be utilised as a gauge for conjugation length. The C=C band of the terpolymers also includes contributions from aggregated (ordered) and unaggregated (amorphous) components, apparent at 1440 cm^{-1} and 1500 cm^{-1}, respectively.[42,43] Given the relatively smaller full-width at half-maximum (FWHM) of the C=C peak in the as-cast films, it can be concluded that both the terpolymer and the **P1–P3**:$PC_{71}BM$ films, in this case, exhibit considerable ordered structures. A blue-shift in this mode suggests a shorter conjugation length, which may result from reduced inter- and/or intrachain order in the terpolymer molecules or from $PC_{71}BM$ inclusion as reported by Tsio and Carach.[42,45] The pristine $PC_{71}BM$ thin films exhibited a predominant band at 1568 cm^{-1} corresponding to the A1 mode.[9,46] This band is visible in the spectra of the **P1–P3**:$PC_{71}BM$ films, confirming the existence of both terpolymer and $PC_{71}BM$.

It is well known that narrower C=C bands reflect a higher degree of chain order.[9,42,47] According to Table 1, the presence of $PC_{71}BM$ interferes negligibly with the ordering of the terpolymer chains since the FWHM of the C=C mode of the pristine terpolymer films is the same within the error margins as that of their corresponding **P1–P3**:$PC_{71}BM$ films.

To obtain deeper insight into the thermally-induced changes in the **P1–P3**:$PC_{71}BM$ structure, the Raman spectra of pristine terpolymers and **P1–P3**:$PC_{71}BM$ thin films were recorded after 3 and 24 h of thermal degradation at 85 °C as depicted in Fig. 3. The symmetric C=C stretching mode experienced negligible shifts in peak position during thermal annealing. In addition, as the annealing time increased, the Raman intensity peaks for the pristine films, except for the pristine **P2** film, increased with negligible broadening due to thermal energy effects, which suggests a decrease in crystallinity especially for the **P1**-based film. For the blended films, an increase in the annealing time led to a negligible change in the Raman peak intensities after 24 h of annealing, which can be attributed to the thermal screening of $PC_{71}BM$.

To further elucidate the thermally-induced molecular ordering evolution in the pristine terpolymers and their blends, the FWHM of the C=C Raman mode (1440 cm^{-1}) and the C=C/C–C intensity ratio ($I_{C=C}/I_{C-C}$) were monitored during the aging as shown in Table 1. The following are key observations:

1. The FWHM of the C=C stretching mode in both pristine and blended films appeared to increase marginally during 3 h of thermal annealing, which can be attributed to a slight increase in thermally induced molecular disorder in the terpolymer chains.[47,48] Furthermore, the FWHM of the C=C stretching mode after 24 h of thermal annealing remained the same within the error margin compared to that of the as-cast film, demonstrating that molecular order was maintained in the samples.[9] Therefore, according to these results, no thermally-induced changes in the molecular order occurred in the pristine and blend films.

2. In accordance with the FWHM measurements, the $I_{C=C}/I_{C-C}$ ratio also exhibited no change within the error margin during the annealing period. Since the conjugated backbone planarity of the terpolymers affects in particular the intensity of the C–C Raman mode as opposed to the C=C mode,[42,44] the

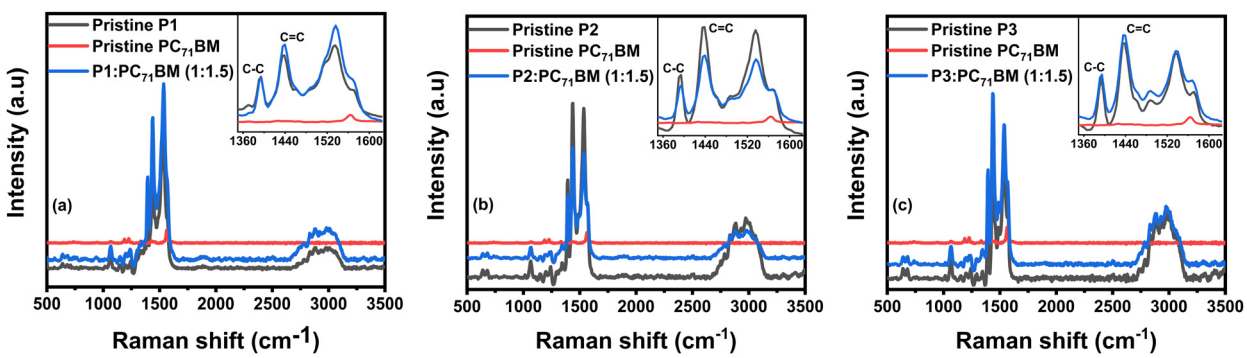

Fig. 2 Raman spectra of as-cast terpolymers (black), $PC_{71}BM$ (red), and **P1–P3**:$PC_{71}BM$ thin films (blue). The spectra were offset for better clarity and the insets display the fingerprints of the respective terpolymers. (a), (b), and (c) represent **P1**-, **P2**-, and **P3**-based films, respectively.

Table 1 FWHM of the C=C Raman peak and C=C/C–C intensity ratio for pristine terpolymers and **P1–P3**:$PC_{71}BM$ thin films, retrieved by fitting the data with a Lorentzian model before and after thermal annealing at 85 °C

	FWHM (cm^{-1})			$I_{C=C}/I_{C-C}$		
Polymer (thin film)	As-cast	3 hours	24 hours	As-cast	3 hours	24 hours
Pristine **P1**	26.94 ± 2.09	27.05 ± 2.30	28.02 ± 2.01	1.54 ± 0.17	1.53 ± 0.18	1.62 ± 0.16
P1:$PC_{71}BM$	30.18 ± 1.86	30.76 ± 1.52	30.14 ± 1.63	1.76 ± 0.18	1.89 ± 0.15	1.78 ± 0.15
Pristine **P2**	21.07 ± 1.05	21.28 ± 1.06	21.34 ± 1.17	1.71 ± 0.11	1.71 ± 0.11	1.70 ± 0.11
P2:$PC_{71}BM$	23.10 ± 1.23	22.39 ± 1.27	22.57 ± 1.01	1.78 ± 0.11	1.73 ± 0.11	1.70 ± 0.07
Pristine **P3**	19.93 ± 1.05	20.26 ± 0.97	20.94 ± 0.91	1.66 ± 0.14	1.74 ± 0.13	1.80 ± 0.12
P3:$PC_{71}BM$	22.01 ± 0.76	22.50 ± 0.60	21.86 ± 0.74	1.79 ± 0.10	1.89 ± 0.09	1.74 ± 0.08

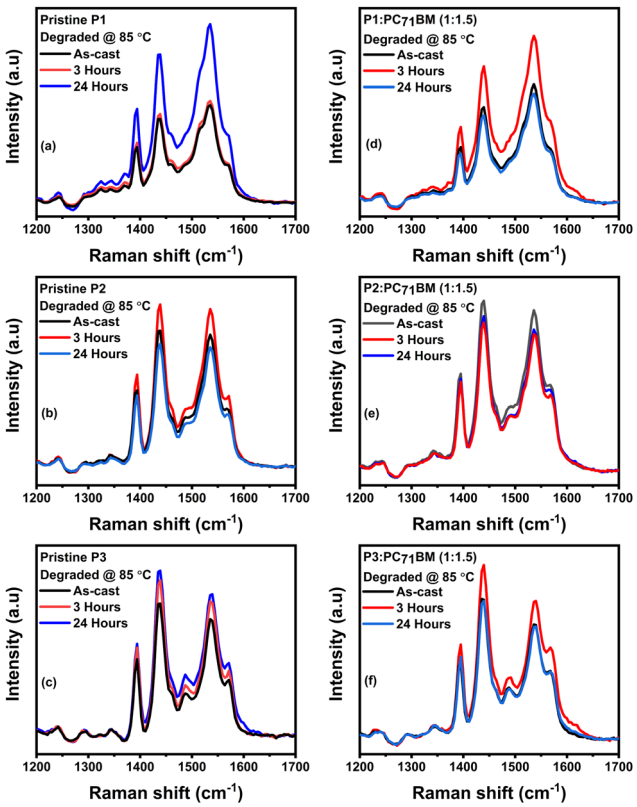

Fig. 3 Raman spectra of pristine terpolymers (a–c) and **P1–P3**:$PC_{71}BM$ thin films (d–f) degraded at 85 °C.

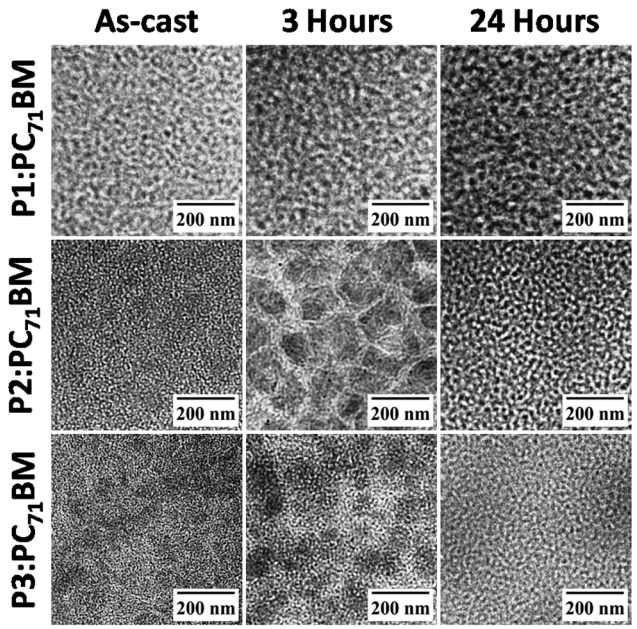

Fig. 4 TEM images of **P1–P3**:$PC_{71}BM$ thin films that underwent no degradation (left) and degraded at 85 °C for 3 hours (middle) and 24 hours (right).

constant $I_{C=C}/I_{C-C}$ ratio after aging confirms that the molecular order of both pristine and blended films is not influenced by annealing. This is consistent with the absence of both spectral shifts and additional Raman peaks in the spectra of pristine and blended films upon thermal degradation, indicating that thermal annealing does not change the molecular and chemical structure of the terpolymers. It can therefore further be concluded that the thermally-induced changes reflected in the absorption spectra (see Fig. 1) are not due to structural modifications in the **P1–P3**:$PC_{71}BM$ films.

3.3 Morphology of the thin films

Aside from photon harvesting, the performance and viability of an OSC active layer are significantly influenced by the active layer's morphological stability, which is an important factor in determining the commercialisation of the device. The morphology of the **P1–P3**:$PC_{71}BM$ thin films was analysed using transmission electron microscopy (TEM), AFM imaging, and XRD (see Fig. 4–6, respectively). The TEM images of the as-cast BHJ films revealed a good interpenetrating network between the terpolymers and $PC_{71}BM$ molecules with small domain sizes, which is beneficial for efficient exciton dissociation[33,36] and the establishment of paths for charge-carrier transport with low recombination rates.[49,50] In the TEM images, $PC_{71}BM$ and terpolymer domains are represented by the dark and bright portions, respectively, due to $PC_{71}BM$'s higher density (1.5 g cm^{-3}) than that of the terpolymers.

By increasing the ratio of TTDPP from **P3** to **P2** to **P1**, the active layer blend morphology of the as-cast films improved (Fig. 4). However, this morphology deteriorated upon thermal annealing. When the annealing period was increased from 3 to 24 h, the dispersion of the donor–acceptor phases became

more compact and the domain sizes increased. This hampers exciton dissociation and carrier transport.[51,52] Ning *et al.*[53] observed a similar phenomenon in PBDTTT-C:$PC_{71}BM$ active layers and attributed the device degradation to inefficient charge generation and imbalance in charge-carrier transport, which is closely associated with the morphological evolution of the active layer with prolonged annealing time. Similarly, the phase segregation between $PC_{71}BM$ and P3HT was also reported to drastically reduce the performance of the device.[54]

After 3 and 24 h of thermal annealing, the active layer based on **P1** displayed a more stable morphology compared to **P2**- and **P3**-based devices, characterised by better intermixing between the donor and acceptor phases and reduced domain sizes. The degradation of the film containing **P2**, which contains a similar ratio of the two acceptors, was faster than that of the film containing **P3** which has the highest FTAZ concentration. Therefore, the phase separation between the terpolymers and $PC_{71}BM$ increased upon thermal annealing. These results suggest that thermal annealing enhanced the phase segregation, probably by means of the crystallisation of terpolymer chains and $PC_{71}BM$ aggregation.[9,51,54,55] Similar results with P3HT:PCBM blends were observed by Yang *et al.*[56] and Hoppe *et al.*[57] Using TEM and SEM they demonstrated that thermal degradation leads to the crystallisation of P3HT chains *via* stacked coplanar conjugated segments and dispersion of PCBM molecules forming large aggregates. A detailed study of the thermal annealing effect on PCBM aggregation was also reported by Kiel *et al.*[55] Based on their neutron reflectivity results, they showed that upon annealing, the PCBM concentration increased at the sample–air interface with little change at the buried interface of the substrate and blend.

To examine the phase segregation in the **P1–P3**:$PC_{71}BM$ blends in more detail, we conducted an AFM analysis of the films. Fig. 5 displays typical AFM images of the films in their as-cast and annealed states after 3 and 24 h of thermal annealing, showing that the morphology of the as-cast **P1–P3**:$PC_{71}BM$ thin films was smooth with well-connected domains. The AFM images

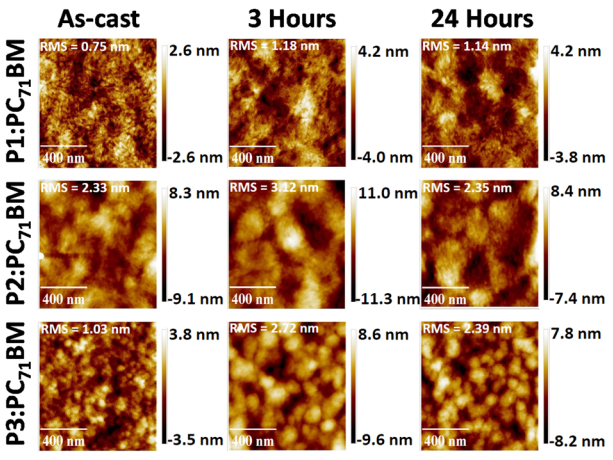

Fig. 5 Atomic force microscopy images (1 × 1 μm^2) of **P1–P3**:$PC_{71}BM$ films showing their root mean square (RMS) surface roughness before degradation (left) and after degradation at 85 °C for 3 h (middle) and 24 h (right).

of the **P1**-based films reveal a more prominent nanofibril production, which is predicted to increase J_{sc} while concurrently lowering V_{oc} in **P1**:$PC_{71}BM$ as-cast-based films.[58] For the **P2**- and **P3**-based films, fibrillar structures can also be seen in Fig. 5, although less prominent than for the **P1**-based films. Comparing the three BHJ films, **P1**, which has the highest TTDPP ratio, displayed the smoothest surface morphology with the least root-mean-square (RMS) of 0.75 nm surface roughness in the as-cast film than **P2**- and **P3**-based BHJ films. The RMS values in this study were similar to our preceding work.[33] The performance of the devices based on these terpolymers blended with $PC_{71}BM$ was reported to decrease with decreasing TTDPP content (**P1** > **P2** > **P3**), consistent with the surface morphology recorded. The main contribution to this improvement was the decrease in J_{sc} from 16.51 to 13.27 to 12.29 mA cm^{-2}.[33] Hence, the thermally-induced evolution of the active layer morphology will undoubtedly affect the performance during aging.

Upon thermal annealing for 3 h, the RMS surface roughness of the **P1**-based film increased significantly to 1.18 nm, but, interestingly, was found to have decreased after 24 h. This trend is most pronounced for **P2**, where the RMS surface roughness after 24 h of thermal annealing is almost the same as that of the as-cast film, in line with the fact that the active layer morphology of OSCs is thermodynamically unstable and usually evolves to a more stable state in time with or without any stressor.[48] It is well known that a lower surface roughness may result in (1) greater interfacial contact between the **P1–P3**:$PC_{71}BM$ active layer and electrodes and (2) a higher probability of dissociation of photogenerated electron and hole pairs at the **P1–P3**:$PC_{71}BM$ interface.[9,51] The increase in RMS surface roughness due to thermal annealing may be a consequence of phase segregation, indicating non-uniform coverage, which may, in turn, affect the interface resistance, short-circuit current and fill factor.[50,51,59] These results are similar to those reported by Veerender *et al.*[9] where they observed the formation of $PC_{71}BM$ aggregates after heating P3HT:$PC_{71}BM$ thin films at temperatures >150 °C.

A qualitative analysis of the formation of PCBM clusters upon thermal degradation of P3HT/PCBM active layers in a previous study[40] also showed that the final morphology of the thin film depended on the thermal annealing strategy. Furthermore, Jung *et al.* recently reported on the superior thermal stability of a 1D/2A terpolymer (PBTPBD) processed with eco-friendly nonhalogenated solvents[16] and attributed the long-term thermal stability of the PBTPBD-50:IT-4F OSC to the excellent miscibility of PBTPBD-50 and IT-4F in *o*-xylene and the suppression of the morphological changes in the photoactive layer upon thermal degradation. Comparing these results with the **P1–P3**:$PC_{71}BM$ active layers in the current study, suggests that polymer **P1** and **P3** have superior miscibility with $PC_{71}BM$ when processed with *o*-DCB. This accounts for their superior morphological and thermal stability, which is closely related to the miscibility between the terpolymers and $PC_{71}BM$ as observed in Fig. 4 and 5.

To support the above observations and also get more information on the structural and molecular packing of the active layers, XRD was done on the **P1–P3**:$PC_{71}BM$ thin films as shown

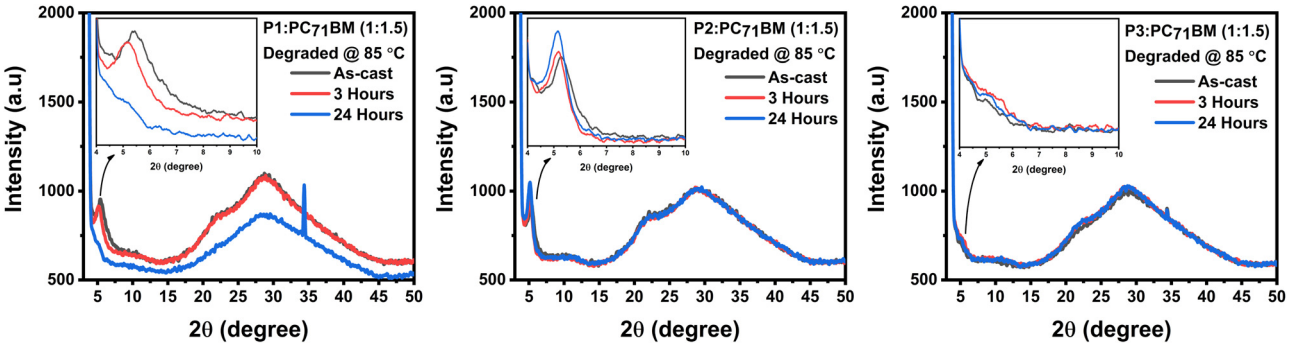

Fig. 6 Thin-film X-ray diffraction patterns of **P1–P3**:$PC_{71}BM$ blends degraded at 85 °C. The insets display the low-angle region of the respective active layers.

in Fig. 6. All the XRD profiles of the **P1–P3**:$PC_{71}BM$ thin films showed a broad hallow between 20° and 40°, which is associated with π−π stacking of the conjugated polymer backbones, indicating intermolecular interaction between the terpolymer backbones.[33] In the low-angle region, only the **P1**- and **P2**-based active layers exhibited a distinct diffraction peak, which indicates the formation of an ordered structure. This peak is, however, very weak for the **P3**-based active layer, indicating a less crystalline nature and a more compatible donor–acceptor blend. The low-angle peak is at 2θ = 5.39° and 5.28°, corresponding to a packing distance of 1.64 nm and 1.67 nm for the as-cast **P1**- and **P2**-based active layers, respectively. In the **P1**-based active layer the packing distance increased with increasing annealing time from 1.64 nm in the as-cast **P1**-based film to 1.71 nm (2θ = 5.17°) after 3 h of thermal annealing, followed by complete degradation of its low-angle peak after 24 h of annealing. This can be attributed to a loss in crystallinity in the **P1**-based active layer upon thermal annealing. However, for the **P2**-based active layer, the thermally-induced increase in the packing distance was much less, from 1.67 nm in the as-cast **P2**-based active layer to 1.70 nm (2θ = 5.18°) and 1.71 nm (2θ = 5.16°) after 3 and 24 h of thermal annealing, respectively, indicating a more stable crystalline nature for the **P2**-based active layer. This thermal stability is more pronounced for the **P3**-based active layer, as we observed no changes in its XRD pattern after thermal annealing, consistent with the Raman results, and confirming the thermal stability of the terpolymers. The forgoing peaks after thermal annealing, especially for the **P1**-based active layer, are the result of $PC_{71}BM$ diffusion within the terpolymer matrix and the formation of larger $PC_{71}BM$ clusters, which affect the miscibility of the donor and acceptor materials, as reflected in our AFM (Fig. 5) and TEM (Fig. 4) images.

3.4 Time-resolved fluorescence measurements of P1–P3:$PC_{71}BM$ thin films

To further understand the impact of thermal degradation on the long-term stability of **P1–P3**:$PC_{71}BM$ active layers, TCSPC was used to determine the fluorescence decay rates of the active layers after thermal annealing. The fluorescence decay trace of each active layer could be best fitted with a two-component exponential model, using an iterative reconvolution least-squares minimisation approach.[60] The goodness-of-fits were confirmed by reduced χ^2 values close to 1, Durbin–Watson parameters close to 2, and the lack of statistical structure in the fitting residuals.[61] It should be noted that a maximum likelihood method as an alternative fitting approach delivered identical results.[62] The time-resolved fluorescence decay traces along with their fits are displayed in Fig. 7 and a summary of the fitting parameters is shown in Table 2.

Two lifetimes were consistently resolved from the best fits using an IRF with a lifetime of 0.01 ns. The short lifetime of ~0.1–0.4 ns can be attributed to the relaxation of excitons that did not reach the donor/acceptor interface due to the presence of carrier traps and recombination centres, while the longer

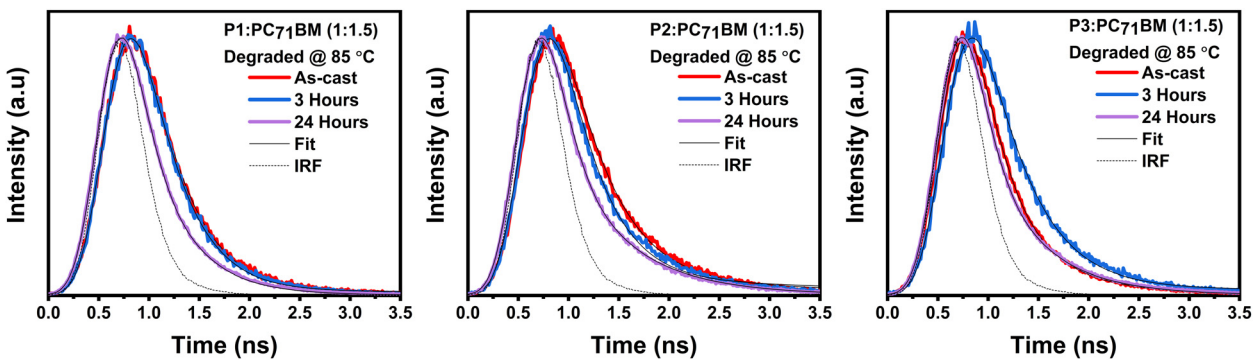

Fig. 7 Time-correlated single-photon counting traces for **P1–P3**:$PC_{71}BM$ thin films degraded at 85 °C.

Table 2 Fluorescence lifetime components (τ_1 and τ_2), corresponding amplitudes (A_1 and A_2), and average amplitude-weighted lifetime ($\langle\tau\rangle$) of **P1–P3**:$PC_{71}BM$ active layers after 0, 3, and 24 h degradation

Thin film	Time (h)	τ_1 (ns)	τ_2 (ns)	A_1 (%)	A_2 (%)	$\langle\tau\rangle$ (ns)
P1:$PC_{71}BM$	As-cast	0.35	6.02	99.0	1.0	0.39
	3	0.32	4.16	99.0	1.0	0.36
	24	0.09	0.42	81.0	19.0	0.15
P2:$PC_{71}BM$	As-cast	0.40	2.66	97.0	3.0	0.47
	3	0.32	3.2	97.0	3.0	0.41
	24	0.10	0.67	85.0	15.0	0.18
P3:$PC_{71}BM$	As-cast	0.19	0.59	82.0	18.0	0.26
	3	0.40	5.56	98.0	2.0	0.48
	24	0.08	0.56	86.0	14.0	0.15

lifetime of $> \sim 1$ ns can be related to the bimolecular recombination of free charge carriers generated following exciton dissociation.[63,64] The lifetime components (τ_1 and τ_2) of each blend are expected to remain largely constant with a change in the corresponding amplitudes indicating a change in the frequency of occurrence of the associating process. Deviations from this trend suggest mixed values. We consider as an example the as-cast **P3**:$PC_{71}BM$ blend, which had the shortest average lifetime. To qualitatively compare the contribution of the two processes associated with the two lifetimes, the lifetime components were fixed at 0.4 ns and 5 ns, respectively, which gave corresponding amplitudes of 99.2% and 0.8%, respectively. Although the fit quality in this case is suboptimal, this alternative fit reveals that the as-cast **P3**:$PC_{71}BM$ blend had a substantial fraction of excitons that did not dissociate, which is consistent with the lower current value we reported.[33]

Thermally-induced morphological evolution has been shown to have a direct impact on charge dynamics.[65] After 24 h of thermal annealing, the average fluorescence lifetime of all three thin films was significantly shortened, with the **P1**-based film affected most and the **P3**-based film affected least, confirming the higher thermal stability of the **P3**:PC71BM blend. The lifetimes of the **P1**- and **P2**-based films decreased monotonously with the thermal annealing time, confirming the decrease in free charge generation and hence the current, consistent with the films' deteriorating morphology, as indicated in the TEM and AFM images by the larger domain sizes due to phase segregation between the donor and acceptor. In contrast, the lifetime of the **P3**-based film increased significantly (by 77%) after 3 h of annealing before dropping upon further annealing. Both lifetime components depend strongly on the diffusion time of free charge carriers; the short lifetime is expected to decrease when the trap density increases, while a decrease in domain sizes and surface roughness will shorten the long lifetime component. The increased average lifetime of the **P3**-based film after 3 h could therefore be the consequence of a temporary increase in charge generation. Similar reports exist in a temporary increase in current and FF during degradation due to a momentarily improved ordering or charge transport.[66,67] Alternatively, it is of note that the average lifetimes of the **P3**-based film are qualitatively anticorrelated with the RMS surface roughness in Fig. 5, which may indicate that thermally-induced changes in the dissociation rate of the **P3**-based film dominated thermally-induced charge generation.

3.5 Correlation between nanostructure and spectroscopy

Based on the analysis of bright-field TEM, AFM, Raman, XRD, time-resolved fluorescence, and absorption results, we evaluate how annealing-induced morphological developments in **P1–P3**:$PC_{71}BM$ active layers would affect potential OSC devices. In the as-cast **P1–P3**:$PC_{71}BM$ thin films, both the terpolymers and $PC_{71}BM$ molecules have disorganised structures and are uniformly distributed across the thin films. When exposed to 3 h of thermal annealing, the terpolymers experienced inter- and intrachain molecular rearrangement without phase segregation (*i.e.*, $PC_{71}BM$ remained evenly distributed).[9,48] This is most evident through the modest increase in the $\pi-\pi^*$ absorption intensity in the pristine terpolymers observed after 3 h of thermal annealing. However, when the annealing period was extended to 24 h, $PC_{71}BM$ molecules began to dissociate from the terpolymer matrix, forming significant $PC_{71}BM$ aggregates, as shown in the TEM (Fig. 4) and AFM (Fig. 5) images. This prevents a homogeneous **P1–P3**:$PC_{71}BM$ blend by inducing a phase separation of $PC_{71}BM$ from the terpolymer matrix, which may result in a reduction of the photogenerated current.[9,48] Therefore, increasing the annealing time above 3 h may result in the formation of larger $PC_{71}BM$ domains, which may grow to be greater than the blend's exciton diffusion length. This might restrict the flow of unbound electrons and holes to the electrodes after exciton dissociation.

In summary, upon thermal annealing, the $PC_{71}BM$ molecules diffuse out of the blend and form sizable aggregates at the sample–air interface, consistent with increased surface roughness as determined from the AFM images (Fig. 5). Despite enhanced interchain molecular ordering within the terpolymer chains after 3 h of thermal annealing, the interfacial area between the terpolymers and $PC_{71}BM$ in the **P1–P3**:$PC_{71}BM$ films decreased dramatically due to the diffusion of $PC_{71}BM$ towards the sample–air interface.[40] The reduced interfacial area may result in a decrease in J_{sc}, while increased RMS surface roughness may degrade the metal electrode and cause inadequate contact between the active layer (**P1–P3**:$PC_{71}BM$ BHJ blend) and the cathode, hence lowering the fill factor.[9] However, unlike other OSC active layer materials that degrade upon thermal annealing, we observed no clear molecular or chemical changes in the **P1–P3**:$PC_{71}BM$ active layers, which is a unique characteristic required for the development of more efficient and stable OSCs. This property is particularly relevant for BHJ OSCs consisting of a blend of electron donor and acceptor materials and relying on efficient charge separation at the donor–acceptor interface.

4 Conclusion

We have demonstrated that by annealing **P1–P3**:$PC_{71}BM$ blend films for different lengths of time, the films develop diverse final morphologies. The annealing temperature and duration

are essential factors taken into consideration when controlling the active layer blend morphology. Our findings suggest that by gradually annealing the blend films, the diffusion of $PC_{71}BM$ molecules to form aggregates may be carefully regulated, resulting in a nanostructure critical to the efficiency of OSCs. For the three terpolymers (**P1–P3**), a distinct relationship between the morphological development of the active layers and their degradation was demonstrated. All three terpolymer active layers exhibited dual crystallisation behavior where terpolymer crystallisation may result in enhanced charge conduction and greater photocurrent output while $PC_{71}BM$ aggregation may result in the formation of clusters, reducing the donor–acceptor interfacial area, which may lead to a decrease in the photogenerated current.

The **P2**-based active layer demonstrated a quick development of $PC_{71}BM$ clusters upon thermal degradation while the **P3**-based film showed the least amount of thermal degradation as confirmed especially by our steady-state absorption, XRD, and time-resolved fluorescence results. The reduced electron acceptor and electron donor interfacial area may therefore result in decreased photocurrent output. The thermal stability of **P1** and **P3** terpolymer films is reflected in the reasonable stability of their absorption spectra, Raman spectra, and microscopic images.

When comparing the three terpolymers, morphological changes in the **P3** active layers are significantly suppressed, resulting in a greater thermal stability of the active layer. Because of its greater FTAZ concentration, its matrix is firmer. This severely limits the possibility of $PC_{71}BM$ molecule movement and segregation, which may result in enhanced thermal stability of the photo-active layer and, as a result, more steady OSC photovoltaic performance.

Author contributions

LTN performed the experimental work and data analysis and wrote the first draft. NAT and TPJK conceptualised and supervised the research and contributed to the data analysis, interpretation, and writing of the manuscript. ZG and WM synthesised the terpolymers and edited the final manuscript.

Conflicts of interest

The authors declare that there is no known conflict of interest in this work.

Acknowledgements

This work is based on the research supported in part by the National Research Foundation of South Africa Grants No. PMDS22063029254 (LTN) and 120387 and 137973 (TPJK), the African Laser Centre Project No. HLHA23X (LTN), the Rental Pool Program of the Council for Scientific and Industrial Research's Photonics Centre, South Africa (LTN and TPJK), and the National Institute for Theoretical and Computational Sciences (NITheCS), South Africa (NAT and TPJK). WM and ZG acknowledge financial support from the International Science Programme (ISP), Uppsala University, Sweden.

References

1 C. W. Tang, *Appl. Phys. Lett.*, 1986, **48**, 183–185.
2 J. Zhang, Y. Han, W. Zhang, J. Ge, L. Xie, Z. Xia, W. Song, D. Yang, X. Zhang and Z. Ge, *ACS Appl. Mater. Interfaces*, 2020, **12**, 57271–57280.
3 Z. Jiang, F. Wand, K. Fukuda, A. Karaki, W. Huang, K. Yu, T. Yokota, K. Tajima, T.-Q. Nguyen and T. Someya, *Proc. Natl. Acad. Sci. U. S. A.*, 2020, **117**, 6391–6397.
4 W. Yang, Z. Luo, R. Sun, J. Guo, T. Wang, Y. Wu, W. Wang, J. Guo, Q. Wu, M. Shi, H. Li, C. Yang and J. Min, *Nat. Commun.*, 2020, **11**, 1218.
5 L.-Y. Su, H.-H. Huang, Y.-C. Lin, G.-L. Chen, W. C. Chen, W. Chen, L. Wang and C.-C. Chueh, *Adv. Funct. Mater*, 2021, **31**, 2005753.
6 L. Duan, Y. Zhang, M. He, R. Deng, H. Yi, Q. Wei, Y. Zou and A. Uddin, *ACS Appl. Mater. Interfaces*, 2020, **12**, 27433–27442.
7 W. Liu, X. Xu, J. Yuan, M. Leclerc, Y. Zou and Y. Li, *Energy Lett.*, 2021, **6**, 598–608.
8 N. Bekri, E. Asmare, W. Mammo and N. A. Tegegne, *Mater. Res. Express*, 2022, **9**, 055502.
9 P. Veerender, V. Saxena, A. K. Chauhan, S. P. Koiry, P. Jha, A. Gusain, S. Choudhury, D. K. Aswal and S. K. Gupta, *Sol. Energy Mater Sol. Cells*, 2014, **120**, 526–535.
10 M. Saito and I. Osaka, *J. Mater. Chem. C*, 2018, **6**, 3668–3674.
11 Y. Xin, G. Zeng, J. OuYang, X. Zhao and X. Yang, *J. Mater. Chem. C*, 2019, **7**, 9513–9522.
12 H. C. Wong, Z. Li, C. H. Tan, H. Zhong, Z. Huang, H. Bronstein, I. McCulloch, J. T. Cabral and J. R. Durrant, *ACS Nano*, 2014, **8**, 1297–1308.
13 N. Li, J. D. Perea, T. Kassar, M. Richter, T. Heumueller, G. J. Matt, Y. Hou, N. S. Güldal, H. Chen, S. Chen, S. Langner, M. Berlinghof, T. Unruh and C. J. Brabec, *Nat. Commun.*, 2017, **8**, 14541.
14 T. E. Kang, K.-H. Kima and J. Kim Bumjoon, *J. Mater. Chem. A*, 2014, **2**, 15252–15267.
15 Z. Li, X. Xu, W. Zhang, X. Meng, W. Ma, A. Yartsev, O. Inganäs, M. R. Andersson, R. A. J. Janssen and E. Wang, *J. Am. Chem. Soc.*, 2016, **138**, 10935–10944.
16 H. Jung, G. Yu, J. Kim, H. Bae, M. Kim, K. Kim, B. Kim and Y. Lee, *Sol. RRL*, 2021, **5**, 2100513.
17 X. Zhang, C. Xiao, A. Zhang, F. Yang, H. Dong, Z. Wang, X. Zhan, W. Li and W. Hu, *Polym. Chem.*, 2015, **6**, 4775–4783.
18 H. A. Um, D. H. Lee, D. U. Heo, D. S. Yang, J. Shin, H. Baik, M. J. Cho and D. H. Choi, *ACS Nano.*, 2015, **9**, 5264–5274.
19 J. H. Park, E. H. Jung, J. W. Jung and W. H. Jo, *J. Adv. Mater.*, 2013, **25**, 2583–2588.

20 B. Sun, W. Hong, Z. Yan, H. Aziz and Y. Li, *J. Adv. Mater.*, 2014, **26**, 2636–2642.
21 R. S. Ashraf, I. Meager, M. Nikolka, M. Kirkus, M. Planells, B. C. Schroeder, S. Holliday, M. Hurhangee, C. B. Nielsen, H. Sirringhaus and I. McCulloch, *J. Am. Chem. Soc.*, 2014, **137**, 1314–1321.
22 H. Choi, S.-J. Ko, T. Kim, P.-O. Morin, B. Walker, B. H. Lee, M. Leclerc, J. Y. Kim and A. J. Heeger, *J. Adv. Mater.*, 2015, **27**, 3318–3324.
23 W. Li, K. H. Hendriks, M. M. Wienk and R. A. J. Janssen, *Acc. Chem. Res.*, 2015, **49**, 78–85.
24 K.-H. Kim, S. Park, H. Yu, H. Kang, I. Song, J. H. Oh and B. J. Kim, *Chem. Mater.*, 2015, **26**, 6963–6970.
25 H.-H. Cho, T. E. Kang, K.-H. Kim, H. Kang, H. J. Kim and B. J. Kim, *Macromolecules*, 2012, **45**, 6415–6423.
26 F. Ullah, S. Qian, W. Yang, M. N. Shah, Z. Zhang, H. Chen and C.-Z. Li, *Chin. Chem. Lett.*, 2017, **28**, 2223–2226.
27 A. Kim, J. H. Lee, H. J. Kim, S. Choi, Y. U. Kim, C. G. Park, C. H. Jeong, M. J. Cho and D. H. Choi, *Synth. Met.*, 2018, **236**, 36–43.
28 M. Lee, T. Kim, H. V. T. Nguyen, H. W. Cho, K.-K. Lee, J.-H. Choi, B. Kim and J. Y. Kim, *RSC Adv.*, 2019, **9**, 42096–42109.
29 J. Hou, M.-H. Park, S. Zhang, Y. Yao, L.-M. Chen, J.-H. Li and Y. Yang, *Macromolecules*, 2008, **41**, 6012–6018.
30 E. Zhu, G. Ge, J. Shu, M. Yi, L. Bian, J. Hai, J. Yu, Y. Liu, J. Zhou and W. Tang, *J. Mater. Chem. A*, 2014, **2**, 13580–13586.
31 L. Huo and J. Huo, *Polym. Chem.*, 2011, **2**, 2453–2461.
32 P. Sista, M. C. Biewer and M. C. Stefan, *Macromol. Rapid Commun.*, 2012, **33**, 9–20.
33 A. Negash, Z. Genene, R. T. Eachambadi, J. Kesters, N. V. D. Brande, J. DHaen, H. Penxten, B. Abdulahi, E. Wang, K. Vandewal, W. Maes, W. Mammo, J. Manca and S. Admassie, *J. Mater. Chem. C*, 2019, **7**, 3375–3384.
34 F. Kyeyune, J. L. Botha, B. van Heerden, P. Maly, R. van Grondelle, M. Diale and T. P. J. Krüger, *Nanoscale*, 2019, **11**, 15139–15146.
35 K. G. Jespersen, W. J. Beeken, Y. Zaushitsyn, A. Yartsev, M. Andersson, T. Pullerits and V. Sundström, *J. Chem. Phys.*, 2004, **121**, 12613–12617.
36 N. A. Tegegne, Z. Abdissa and W. Mammo, *Polym. J.*, 2021, **13**, 1151–1164.
37 B. S. Desalegn, N. Bekri, F. G. Hone, D. M. Andoshe, W. Mammo, Z. Abdissa, G. Bosman and N. A. Tegegne, *Mater. Today Commun.*, 2021, **29**, 102803.
38 O. V. Mikhnenko, H. Azimi, M. Scharber, M. Morana, P. W. Blom and M. A. Loi, *Energy Environ. Sci.*, 2012, **5**, 6960–6965.
39 P. Henriksson, C. Lindqvist, B. Abdisa, E. Wang, Z. George, R. Kroon, C. Muller, T. Yohannes, O. Inganddotas and M. R. Andersson, *Sol. Eneregy Mater. Sol. Cells*, 2014, **130**, 138–143.
40 O. Oklobia and T. S. Shafia, *Sol. Energy Mater Sol. Cells*, 2013, **117**, 1–8.
41 M. O. Reese, A. M. Nardes, B. L. Rupert, R. E. Larsen, D. C. Olson, M. T. Lloyd, S. E. Shaheen, D. S. Ginley, G. Rumbles and N. Kopidakis, *Adv. Funct. Mater.*, 2010, **20**, 3476–3483.
42 W. T. Tsoi, D. T. James, J. S. Kim, P. G. Nicholson, C. E. Murphy, D. D. C. Bradley, J. Nelson and J. S. Kim, *J. Am. Chem. Soc.*, 2011, **133**, 9834–9843.
43 Y. Gao and J. K. Grey, *J. Am. Chem. Soc.*, 2009, **131**, 9654–9662.
44 A. M. Ballantyne, T. A. M. Ferenczi, M. C. ampoy Quiles, T. M. Clarke, A. Maurano, K. H. Wong, W. Zhang, N. S. tingelin Stutzmann, J. S. Kim, D. D. C. Bradley, J. R. Durrant, I. McCulloch, M. Heeney, J. Nelson, S. Tierney, W. Duffy, C. Mueller and P. Smith, *Macromolecules*, 2010, **43**, 1169–1174.
45 C. Carach, I. Riisness and M. J. Gordon, *Appl. Phys. Lett.*, 2012, **101**, 083302–083306.
46 G. Sun and M. Kertesz, *J. Phys. Chem. A*, 2002, **106**, 6381–6386.
47 S. Miller, G. Fanchini, Y. Y. Lin, C. Li, C. W. Chen, W. F. Su and M. Chhowalla, *J. Mater. Chem.*, 2008, **18**, 306–312.
48 P. Cheng and X. Zhan, *Chem. Soc. Rev.*, 2016, **45**, 2544–2582.
49 H. Guo, T. Shen, F. Wu, G. Wang, L. Ye, Z. Liu, B. Zhao and S. Tan, *RSC Adv.*, 2016, **6**, 13177–13184.
50 T. H. Lee, S. Y. Park, B. Walker, S.-J. Ko, J. Heo, H. Y. Woo, H. Choi and J. Y. Kim, *RSC Adv.*, 2017, **7**, 7476–7482.
51 U. Bothra, N. Jain, A. C. Y. Liu, A. Kala, W. Huang, X. Jiao, E. Gann, V. G. Achanta, C. R. McNeill and D. Kabra, *ACS Appl. Nano Mater.*, 2020, **3**, 11080–11089.
52 Y. Yan, X. Liu and T. Wang, *J. Adv. Mater.*, 2017, **29**, 1601674.
53 Y. Ning, L. Lv, Y. Lu, A. Tang, Y. Hu, Z. Lou, F. Teng and Y. Hou, *Int. J. Photoenergy*, 2014, 2014.
54 Y. A. Mohammed, F. G. Hone, G. T. Mola and N. A. Tegegne, *Phys. B*, 2023, **653**, 414666.
55 J. W. Kiel, B. J. Kirby, C. F. Majkrzak, B. B. Maranville and M. E. Mackay, *Soft Matter*, 2010, **6**, 641–646.
56 X. Yang, J. Loos, S. C. Veenstra, W. J. H. Verhees, M. M. Wienk, J. M. Kroon, A. J. Michels and R. A. J. Janssen, *Nano Lett.*, 2005, **5**, 579–583.
57 H. Hoppe, M. Niggemann, C. Winder, J. Kraut, R. Hiesgen, A. Hinsch, D. Meissner and N. S. Sariciftci, *Adv. Funct. Mater.*, 2004, **14**, 1005–1011.
58 A. K. K. Kyaw, D. H. Wang, C. Luo, Y. Cao, T.-Q. Nguyen, G. C. Bazan and A. J. Heeger, *Adv. Energy Mater.*, 2014, **4**, 1301469.
59 W. Li, Y. An, M. M. Wienk and R. A. J. Janssen, *J. Mater. Chem. A*, 2015, **3**, 6756–6760.
60 A. Grinvald and I. Z. Steinberg, *Anal. Biochem.*, 1974, **59**, 583–598.
61 J. L. Botha, B. van Heerden and T. P. J. Krüger, *arXiv*, 2024, preprint, arXiv:2404.18945 [physics.bio-ph], 1–22, DOI: **10.48550/2404.18945**.
62 Z. Bajzer, T. M. Therneau, J. C. Sharp and F. G. Prendergast, *Eur. Biophys. J.*, 1991, **20**, 247–262.
63 R. Suthar, H. Dahiya, A. K. Singh, G. D. Sharma and S. Karak, *ACS Appl. Mater. Interfaces*, 2023, **15**, 3214–3223.

64 N. A. Tegegne, Z. Abdissa, W. Mammo, T. Uchiyama, Y. Okada-Shudo, F. Galeotti, W. Porzio, M. R. Andersson, D. Schlettwein and V. Vohra, *et al.*, *J. Phys. Chem. C*, 2020, **124**, 9644–9655.

65 S. Zhan, Q. Li, F. Tan, C. Yang, Y. Wu, X. Jia, C. Li, K. Liu, S. Qu and Z. Wang, *et al.*, *J. Power Sources*, 2022, **532**, 231351.

66 T. S. Glen, N. W. Scarratt, H. Yi, A. Iraqi, T. Wang, J. Kingsley, A. R. Buckley, D. G. Lidzey and A. M. Donald, *J. Polym. Sci., Part B: Polym. Phys.*, 2016, **54**, 216–224.

67 H. Saito, T. Uchiyama, Y. Okada-Shudo, W. Mammo, T. P. J. Krüger, V. Vohra and N. A. Tegegne, *J. Phys. D: Appl. Phys.*, 2022, **56**, 044007.

